Computers, Materials & Continua CMC, vol.65, no.3, pp.2123-2141, 2020

A Numerical Gas Fracturing Model of Coupled Thermal, Flowing and Mechanical Effects

Dan Ma[1, 2], Hongyu Duan[2], Qi Zhang[3, *], Jixiong Zhang[1], Wenxuan Li[2], Zilong Zhou[2] and Weitao Liu[4]

Abstract: Gas fracturing, which overcomes the limitation of hydraulic fracturing, is a potential alternative technology for the development of unconventional gas and oil resources. However, the mechanical principle of gas fracturing has not been learned comprehensively when the fluid is injected into the borehole. In this paper, a damage-based model of coupled thermal-flowing-mechanical effects was adopted to illustrate the mechanical principle of gas fracturing. Numerical simulation tools Comsol Multiphysics and Matlab were integrated to simulate the coupled process during the gas fracturing. Besides, the damage evolution of drilling areas under several conditions was fully analyzed. Simulation results indicate that the maximum tensile stress, which occurs in the upper and lower of the injection hole, decreases with the increase of the tectonic stress coefficient (TSC). As the TSC increases, shear fractures increase, a crushed area is gradually formed and the seepage area increases rapidly. The influence of TSC on fracture expansion is concluded as follows: with the decrease of TSC, the relative width of fractures decreases whilst the depth increases. It indicates that thermal stress and pore pressure promote the expansion of tensile fractures but restrain the expansion of shear fractures. Therefore, a relatively lower injection gas pressure is required to obtain the same degree of fracturing with a coupled thermal gradient.

Keywords: Gas fracturing, thermal-flowing-mechanical model, damage evolution, numerical model.

1 Introduction

With the massive global consumption of conventional oil and gas resources, unconventional energy plays an increasingly important role in maintaining a diverse

[1] State Key Laboratory of Coal Resources and Safe Mining, School of Mines, China University of Mining & Technology, Xuzhou, 221116, China.

[2] School of Resources & Safety Engineering, Central South University, Changsha, 410083, China.

[3] Beijing Research Institute of Uranium Geology, Beijing, 100029, China.

[4] State Key Laboratory of Mining Disaster Prevention and Control, Shandong University of Science and Technology, Qingdao, 266590, China.

[*] Corresponding Author: Qi Zhang. Email: zhangqi428@126.com.

Received: 08 May 2020; Accepted: 26 June 2020.

(hence affordable) and secure energy supplies [Lu and Zhao (2015)]. Among these unconventional resources, tight sandstone gas offers very rich reserves and has successfully been exploited for commercial use in North America in recent years [Davis, Nguyen, McClung et al. (2018)]. The successful exploitation of tight sandstone gas has revolutionized the energy cost in the US and economically stimulated major manufacturing industries. However, unconventional gas reservoirs, such as tight gas sandstone wells, have the extremely low porosity and permeability (less than 1 mD), and it is difficult to directly exploit these unconventional gas reservoirs for the commercial use [Pan and Connell (2012)]. Hence, the majority of tight sandstone gas wells need to be reformed to enhance natural gas production.

Hydraulic fracturing is the most common reforming method for tight sandstone gas exploitation. In this process, the high-pressure water is sent to the borehole to produce fractures around the borehole, resulting in a significant improvement in permeability [Ma, Duan, Li et al. (2019); Ma, Wang, Cai et al. (2019)]. Many numerical models have been established to study the hydraulic fracturing, such as phase field method [Zhou, Zhuang and Rabczuk (2019)], cracking particle method [Rabczuk and Belytschko (2004)] and immersed particle method [Rabczuk, Gracie, Song et al. (2010)]. In the phase field method, the fracture behavior is controlled through the phase field model, and the fracture propagation is driven by the elastic energy; in the cracking particle method and immersed particle method, the fluid is allowed to flow through openings between fracture surfaces when the structure fails. Although hydraulic fracturing is widely used in the gas industry, it has many limitations. First, hydraulic fracturing requires a large amount of water, which limits the application for tight sandstone gas wells in water-deficient areas [Osborn, Vengosh, Warner et al. (2011)]. Second, clays around the fracture expand as water invades the formation, which results in the decrease of rock permeability and the reduction of gas productivity [Li, Li, Wang et al. (2016)]. Third, hydraulic fracturing may lead to wastewater treatment and groundwater water pollution problems [Ma, Duan, Liu et al. (2020); Ma, Wang and Li (2019)].

To this end, many researchers [Gu, Tao, Li et al. (2020); Zhang, Ma, Liu et al. (2019); Liu, Xie, Yao et al. (2019)] have studied the gas fracturing methods. Jia et al. [Jia, Lu, Elsworth et al. (2018)] conducted a supercritical carbon dioxide fracturing test on rock samples to study crack surface characteristics and permeability evolution during gas fracturing. By a self-developed true triaxial gas fracturing system, Lu et al. [Lu, He, Wu et al. (2020)] studied the AE activities, fracture propagation and spatial morphologies during the fracturing process. Lisjak et al. [Lisjak, Kaifosh, He et al. (2017)] simulated gas fracturing processes in discontinuous, porous rock masses through a Finite-Discrete Element Method. Shen et al. [Shen and Shi (2016)] outlined a two-dimensional Displacement Discontinuity Method to study the interactions of the fluid flow and rock mass deformation during fracturing processes. Guo et al. [Guo, Qu, Gong et al. (2016)] promoted a three-dimensional Extended Finite Element Method fracturing numerical model by the Abaqus Software; and comprehensively analyzed the influence of horizontal in-situ stress differences, azimuth, and lengths of radial boreholes. Nikolskiy et al. [Nikolskiy, Zammarchi, Mogilevskaya et al. (2016)] used a three-dimensional Boundary Element Method to investigate the fracturing process of fractures interacting with a cylindrical uniformly pressurized borehole.

The above work provides consults for gas fracturing, however, the thermal effect on gas fracturing is ignored in the above works. The gas fracturing for tight sandstone gas exploitation is a thermal-flowing-mechanical (TFM) coupled process. Many numerical methods, such as the Discrete Element Method and Particle Flow Method, have been used to solve the coupled TFM problems [Wang, Hu, Elsworth et al. (2017); Zhang, Ma, Liu et al. (2019); Wang, Shi, Liu et al. (2016)]. Nevertheless, the TFM coupled process in gas fracturing needs to be further studied.

In this paper, a numerical solution is proposed for simulating the coupled relationship between solid mechanics, gas seepage, and thermal behavior; and a fully-coupled damage-based TFM model is also established. In view of the complexity of the underground environment during gas fracturing, the TFM approach can give a detailed insight into the coupled response of the sandstone rock. In this study, the model and equations are prepared by Matlab code and calculated by Comsol Multiphysics. Finally, the damage evolution of the drilling area under different gas fracturing conditions is studied and discussed.

2 Governing equations

In this paper, governing equations are based on the macroscopic scale, obtained with some basic assumptions: (a) sandstone rock is a heterogeneous, isotropic and elastic continuum material, (b) the strain and displacement of sandstone are small, (c) the post-peak stress-strain relation of sandstone satisfies the damage model, and (d) the injection gas for the fracturing is ideal gas. Under these hypotheses, a series of coupled equations are established to describe the deformation of rock, gas seepage in rock, and the process of heat transfer in the gas fracturing.

2.1 Mechanical equilibrium and damage evolution equations

Since sandstone rock is assumed to be an elastic continuum material, its deformation will obey the physical equations of elasticity. Due to the thermal conduction and gas seepage, the modified physical equation is as follows [Cao, Zhou, Zhang et al. (2015)],

$$\sigma_{ij} = 2G\varepsilon_{ij} + 2G\frac{\nu}{1-2\nu}\varepsilon_v\delta_{ij} - \alpha p\delta_{ij} - K\alpha_T T\delta_{ij} \tag{1}$$

where σ_{ij} is the component of the total stress tensor; $G = E/2(1+\nu)$ is the shear modulus of the rock; E is the Young's modulus of rock; ν is the Poisson's ratio of rock; ε_{ij} is the component of total strain tensor; $\varepsilon_v = \varepsilon_{11} + \varepsilon_{22} + \varepsilon_{33}$ is volumetric strain; δ_{ij} is the Kronecker delta; $\alpha = 1 - K/K_s$ is the Biot coefficient; $K = E/3(1-2\nu)$ is the bulk modulus of rock; K_s is the bulk modulus of rock grains; p is the pore pressure; α_T is the thermal expansion coefficient of rock; T is the absolute temperature.

The geometric equation of the rock deformation is shown by Eq. (2).

$$\varepsilon_{ij} = (u_{i,j} + u_{j,i})/2 \tag{2}$$

Putting the Eqs. (1) and (2) into the equilibrium equation, then the modified Navier-type equation is deduced as Eq. (3).

$$Gu_{i,jj}+\frac{G}{1-2\nu}u_{j,ji}-\alpha p_{,i}-K\alpha_T T_{,i}+f_i=0 \tag{3}$$

where u_i and u_j are the components of displacement in i and j direction, respectively; f_i is the component of the net body force.

To describe the damage condition of rock, when the rock matrix begins to fracture, a damage variable D *is* introduced. If the stress of rock meets the maximum tensile stress criterion, tensile damage occurs; if the stress of rock meets the Mohr-Coulomb criterion, shear damage occurs. Since the tensile strength of the rock is far smaller than the compressive strength, the tensile damage of rock is given priority. The tensile stress criterion and the Mohr-Coulomb criterion can be described by Eqs. (4) and (5).

$$F_1=\sigma_1-f_t=0 \tag{4}$$

$$F_2=-\sigma_3+\sigma_1\frac{1+\sin\varphi}{1-\sin\varphi}-f_c=0 \tag{5}$$

where σ_1 and σ_3 are the axial and radial principal stresses, respectively; φ is the internal friction angle; f_t and f_c are the tensile strength and the compressive strength, respectively.

According to the theory of damage mechanics, when damage occurs, the elastic modulus and the strength of the rock reduces correspondingly. The variation of elastic modulus and strength (with damage) is expressed by Eqs. (6)-(8) [Zhang, Ma, Liu et al. (2019)].

$$E=(1-D)E_0 \tag{6}$$

$$f_t=(1-D)f_{t0} \tag{7}$$

$$f_c=(1-D)f_{c0} \tag{8}$$

where E_0 is the initial Young's modulus of rock; f_{t0} and f_{c0} are the initial tensile strength and compressive strength of rock, respectively; D is the damage variable, which can be calculated in line with Eq. (9) [Wei, Zhu, Yu et al. (2015)].

$$D=\begin{cases}0 & F_1<0,F_2<0\\ 1-\left|\dfrac{\varepsilon_t}{\varepsilon_1}\right|^2 & F_1=0,dF_1>0\\ 1-\left|\dfrac{\varepsilon_c}{\varepsilon_3}\right|^2 & F_2=0,dF_2>0\end{cases} \tag{9}$$

where ε_1 and ε_3 are the axial and radial principal strains, respectively; ε_t and ε_c are the tensile strain and the compressive strain.

2.2 Gas seepage

The gas continuity equation during gas seepage in the rock is described by Eq. (10).

$$\frac{\partial m}{\partial t}+\nabla(\rho_g q_g)=Q_m \tag{10}$$

where m represents the gas mass per volume of rock; t is the time variable; ρ_g is the density of the gas; q_g is the seepage velocity of the gas; Q_m is the source origin.

According to Darcy's Law, the seepage velocity of gas is can be expressed by Eq. (11).

$$q_g=-\frac{k}{\mu}\nabla p \tag{11}$$

where k represents the permeability of the gas; μ is the dynamic viscosity coefficient.

Since the gas is assumed to be an ideal gas, its state equation can be expressed as follows:

$$\rho_g=\frac{pM_g}{RT} \tag{12}$$

where M_g represents the relative molecular mass of gas; R is the constant value of ideal gas.

After Eqs. (11) and (12) are substituted into (10), the gas continuity term can be deduced using Eq. (13).

$$\frac{M_g}{RT}\frac{\partial(p\phi)}{\partial t}-\frac{M_g}{RT}\nabla(\frac{k}{\mu}p\nabla p)=Q_m \tag{13}$$

Considering that both the temperature and the mechanical (solid) behavior has a significant influence on the evolution of the porosity in sandstone rocks, the dynamic porosity evolution can be defined by Eq. (14) [Xia, Zhou, Liu et al. (2014)]:

$$\phi=\alpha-(\alpha-\phi_0)\exp[\varepsilon_{v0}-\varepsilon_v+\alpha_T(T-T_0)-(p-p_0)/K_s] \tag{14}$$

where ϕ represents the porosity of the rock; ϕ_0 is the initial rock porosity; T_0 is the initial temperature; p_0 is the initial pore pressure.

The evolution of permeability following a cubic law is described in Eq. (15) [Zhang, Liu and Elsworth (2008)],

$$k=k_0\{\frac{\alpha-(\alpha-\phi_0)\exp[\varepsilon_{v0}-\varepsilon_v+\alpha_T(T-T_0)-(p-p_0)/K_s]}{\phi_0}\}^3 \tag{15}$$

2.3 Energy conservation

Based on the conservation of energy principle [Sokolnikoff and Specht (1956)], the energy conservation equation is written in Eq. (16),

$$(\rho C)_M\frac{\partial T}{\partial t}-\rho_g C_g\nabla T(\frac{k}{\mu}\nabla p)+TK\alpha_T\frac{\partial\varepsilon_v}{\partial t}=\lambda_M\nabla^2 T+Q \tag{16}$$

where the second and third items are additional from the gas seepage and solid deformation during gas fracturing; the second item ($\rho_g C_g \nabla T\left(\frac{k}{\mu}\nabla p\right)$) is heat exchange from gas flow, and the third item ($TK\alpha_T \frac{\partial \varepsilon_v}{\partial t}$) is the energy from elastic deformation and fracture dissipation; $(\rho C)_M = \phi(\rho_g C_g) + (1-\phi)(\rho_s C_s)$ is the heat capacity of the rock; C_g and C_s are the heat capacity at a constant pressure of the gas (g) and specific heat capacity of rock (s); $\lambda_M = \phi\lambda_g + (1-\phi)\lambda_s$ is the heat transfer coefficient of the media, where λ_g and λ_s are the gas and the rock heat transfer coefficients, respectively. Q is the external heat source supplied to the system.

Based on the mechanical equilibrium equations, gas seepage equations and energy conservation equations are established above, and the coupling relationship between all three is described, as shown in Fig. 1.

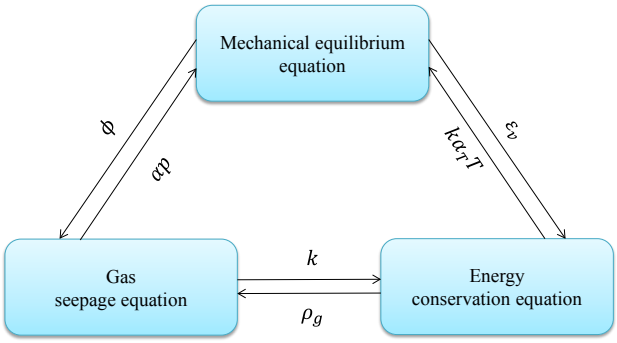

Figure 1: Coupling relationship between solid-gas-temperature physics

2.4 Characterization of rock heterogeneity

Since rock is heterogeneous in the natural world, fractures contain spatial variations in physical properties and chemical composition. The heterogeneity of rock is represented by the Weibull distribution function in this work. The Weibull statistical distribution and the probability density function are described in Eq. (17) [Zhang, Ma, Liu et al. (2019)].

$$f(x,\bar{x},\eta) = \frac{\eta}{\bar{x}}\left(\frac{x}{\bar{x}}\right)^{\eta-1} \exp\left[-\left(\frac{x}{\bar{x}}\right)^{\eta}\right] \tag{17}$$

where x represents the mechanical parameter of rock; $\bar{x}$ represents the average mechanical parameter of rock; η represents the coefficient of heterogeneity.

3 Model validation

The effectiveness of the proposed model should be validated before it is used to simulate the damage evolution under the TFM condition. In this part, the numerical model is verified through a comparison with a theoretical solution. In 1957, Hubbert et al.

[Hubbert and Willis (1957)] proposed an analytical solution for forecasting the breakdown pressure in hydraulic fracturing as shown in Eq. (18),

$$p_b = \sigma_t - \sigma_1 + 3\sigma_3 - p_0 \tag{18}$$

where p_b is the breakdown pressure; σ_t is the tensile strength of the rock; σ_1 and σ_3 are the maximum and minimum principal stress, respectively; p_0 is the initial pore pressure.

In this part, a 2 m×2 m rectangle with a 0.4 m hole at the center is used as the numerical sample for validation, as shown in Fig. 2(a). For the parameters, the average tensile strength and compressive strength of the specimen are 5.9 MPa and 59.4 MPa, respectively, the average elastic modulus of the numerical specimen is 35.9 GPa, and the initial pore pressure is 1 MPa. The horizontal stress is set as 25 MPa, and the vertical stress is varying from 10 MPa to 25 MPa. A tectonic stress coefficient $\lambda(\sigma_x/\sigma_y)$ is introduced in this part, and breakdown pressures under different tectonic stress conditions are obtained with the proposed model.

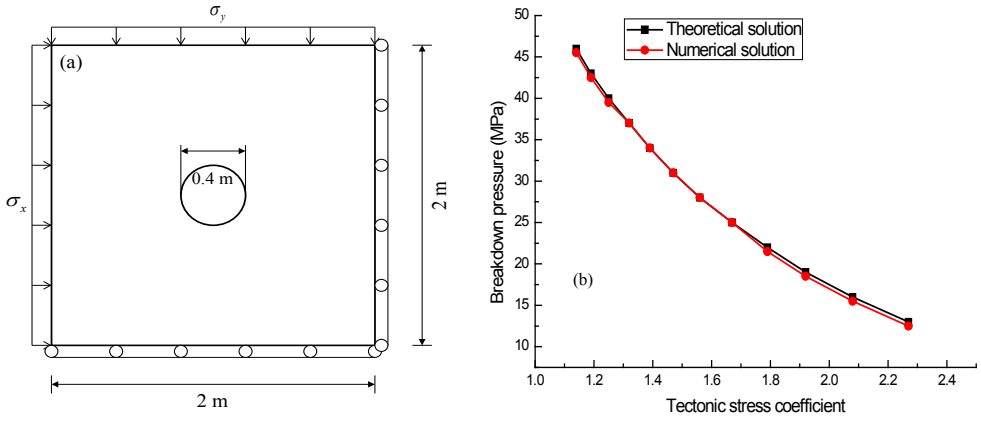

Figure 2: Numerical sample for validation. (a) Numerical sample; (b) The comparison of the numerical and theoretical solution

Fig. 2(b) shows the comparison of the breakdown pressure under different tectonic stress coefficients by the numerical simulation and theoretical solution. The research results indicate that the breakdown of numerical simulation agrees well with that obtained from the theoretical solution. Therefore, the proposed numerical model can be employed to simulate the gas fracturing under the TFM condition.

4 Damage evolutions under coupled TFM condition

In this work, a 2 m×2 m rectangle with a 0.4 m hole at the center is used as the calculation model. The boundary conditions and the initial conditions are defined and illustrated in Fig. 3(a). The calculation parameters used in this numerical simulation are listed in Tab. 1. To facilitate the analysis and calculation of the problem, the calculation model is simplified as a plane strain problem and solved by Comsol Multiphysics. All modules are written in strong forms and solved based on standard finite element

discretization in space domain and finite difference discretization in the time domain. The domain is discretized with 11724 free triangular elements (this number of elements can effectively avoid the dependence of the numerical results on the mesh [Wei, Zhu, Yu et al. (2015)]) and the linear Lagrange shape function is adopted. A fully coupled scheme is employed to solve the coupled system of equations in Comsol solver. The Backward Differentiation Formulas (BDF) method is used for time integration, in which maximum and minimum BDF orders are set to be 5 and 1, respectively. The Newton-Raphson approach is adopted to obtain the residual of the discrete equations, respectively. Based on the above model setting, four different situations are analyzed: (i) damage zone evolution under varied mechanical boundaries; (ii) damage zone evolution under varied gas pressure; (iii) damage zone evolution under varied temperature; (iv) damage zone evolution under coupled gas-temperature-mechanical conditions.

Table 1: Parameters of rock and gas used in the numerical simulations

Parameter	Unit	Value
Young's modulus of rock, E	GPa	36
Poisson's ratio of rock, ν	–	0.225
Density of rock, ρ_s	kg/m^3	2600
Biot coefficient, α	–	0.1
Thermal expansion coefficient of rock, α_T	K^{-1}	2.4×10^{-5}
Internal friction angle of rock, φ	rad	0.117×pi
Uniaxial compressive strength of rock, f_c	MPa	60
Uniaxial tensile strength of rock, f_t	MPa	6
Relative molecular mass of gas, M_g	g/mol	44
The constant value of ideal gas, R	J/(mol•K)	8.31
Dynamic viscosity coefficient, μ	Pa•s	1.79×10^{-5}
Initial rock porosity, ϕ_0	–	0.01
Initial value of volumetric strain of rock, ε_{v0}	–	0
Initial value of temperature, T_0	K	350
Initial value of pore pressure, p_0	MPa	20
Initial value of permeability, k_0	m^2	10^{-18}
Heat transfer coefficient of rock, λ_s	J•(m•s•K)$^{-1}$	0.2
Heat transfer coefficient of gas, λ_g	J•(m•s•K)$^{-1}$	0.014
Specific heat capacity of rock, C_s	J/(kg•K)	1.25×10^3
Heat capacity at constant pressure of gas, C_g	J/(kg•K)	8.4×10^2

The calculation process is illustrated by the logic flow chart in Fig. 3(b), and the basic procedure is summarized as follows.

(i) The calculation geometry is discretized into 40401 (201×201) elements. Then, the initial mechanical, hydraulic and thermal properties are defined, and the initial boundary

conditions are applied. In this procedure, the parameters satisfied the Weibull distribution are produced in Matlab, then imported in Comsol Multiphysics.

(ii) A coupled analysis is conducted by numerical solver Comsol Multiphysics, and the stress, strain, pore pressure and temperature for each of the elements are obtained.

(iii) All the calculation elements will be checked whether they are damaged, according to the criterion Eqs. (4) and (5).

(iv) Strains of the damaged elements are adopted in Eq. (9) to calculate the damage variable. Then, the parameters of these elements are modified by the following Eqs. (6)-(8).

(v) Numerical simulation is performed with the updated parameters, and the simulation results are compared with the former step results. If the damage expands, Steps (iii)-(v) will be repeated, otherwise, Step (vi) is adopted.

(vi) The boundary conditions are updated in the next load increment.

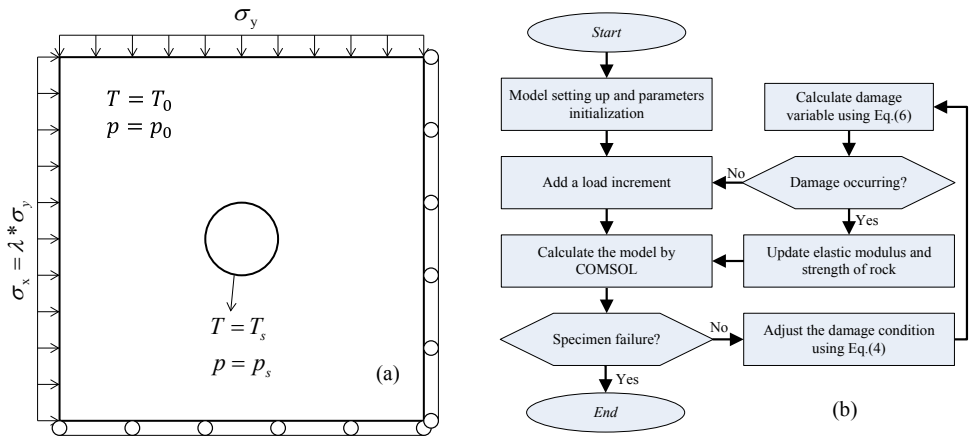

Figure 3: Numerical model and chart. (a) Calculation model and its boundary and initial conditions; (b) Calculation chart of the numerical simulation

4.1 Damage evolution under varied mechanical boundaries

To understand the damage evolution within the drilling area under different tectonic stress conditions, a series of numerical simulations under different stress conditions are carried out. β is the tectonic stress coefficient, representing the ratio of horizontal stress to vertical stress, and its values were 0.1, 0.25, 0.5, 0.75, 1.0. In the numerical calculations, the increment of vertical boundary stress is $\Delta\sigma_y$ =1 MPa and the horizontal boundary stress increases with the tectonic stress coefficient, β. It should be noted that gas pressure and temperature remain constant at this point (T =350 K, p =20 MPa).

Fig. 4 shows the damage evolution within the drilling area. To distinguish the tensile damage and shear damage, the values for tensile damage are negative whilst the values for shear damage are positive. Fig. 4(a) shows the evolution of the drilling area when the tectonic stress coefficient β =0.1. Here, the tensile damage first appears above and below the borehole (at Step 11), at which point the vertical boundary stress is 11 MPa. At Step 23, the shear damage

occurs at the left and right side of the borehole, and the tensile damage occurs at the above and below of the borehole, then fractures are gradually formed. As the boundary stress increases, the tensile fractures propagate in the direction away from the borehole, and the shear damage occurs, leading to the formation of the fractures (at Step 32). Eventually, tensile fractures and shear fractures propagate gradually until unstable failure occurs (at Step 33).

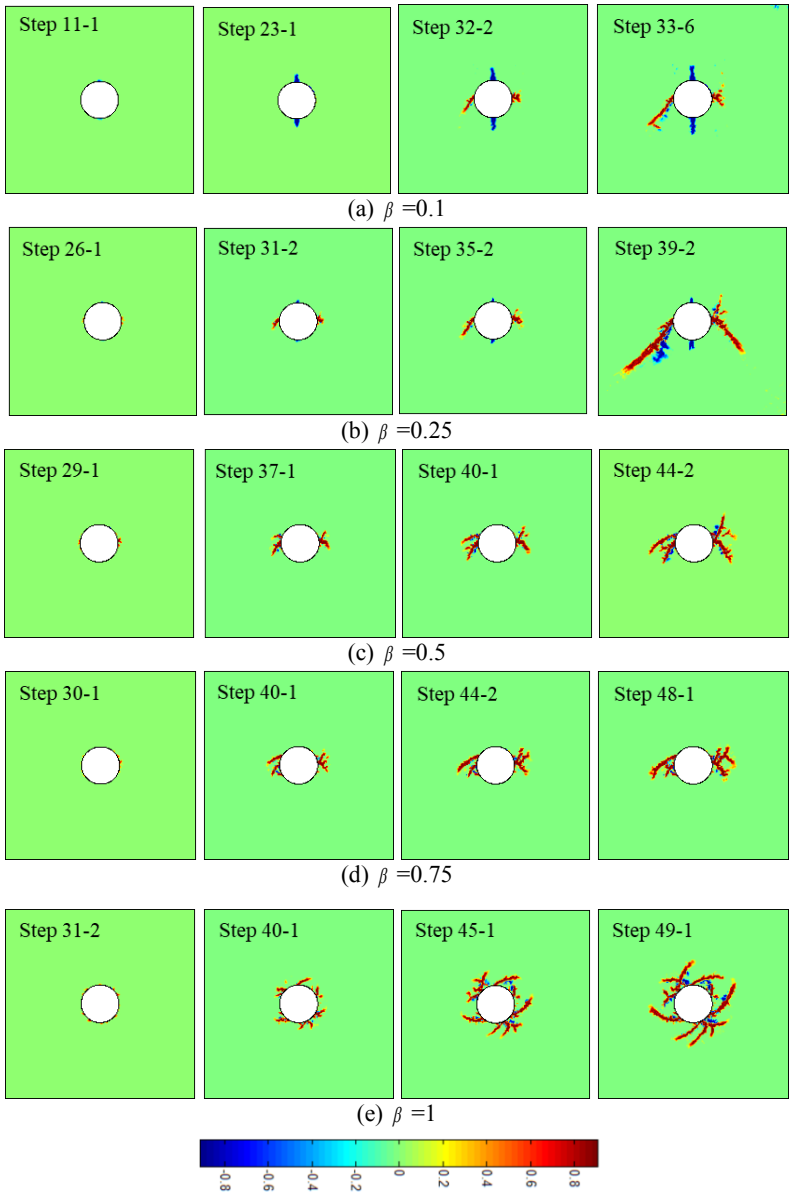

Figure 4: Damage evolution of drilling area under different tectonic stress coefficients β (positive value denotes shear damage, negative value denotes tensile damage)

As the tectonic stress coefficient increases to β=0.25, shear damage first emerges at the left and right side of the borehole (at Step 26), and tensile damage can be observed at Step 31 above and below of the borehole. As the boundary stress increases (at Steps 35 and 39), the tensile damage propagates towards the top and bottom of the specimen, resulting in the primary formation of fractures.

The seepage area under different vertical boundary stress is depicted in Fig. 5. It is noted that, with the appearance of the damage area, the permeability of that area increases correspondingly. Thus, the damaged area is treated as the seepage area in this study. As shown in Fig. 5, when specimens fail and the tectonic stress coefficient β=0.25, the seepage zone is 0.16 m^2; when the tectonic stress coefficient β=0.1, the seepage zone is 0.073 m^2. The fractures in Fig. 4(b) are much smaller than those in Fig. 4(a), and the shear damage expands along the diagonal direction to form further fractures. A similar damage pattern can be observed in both Figs. 4(a) and 4(b).

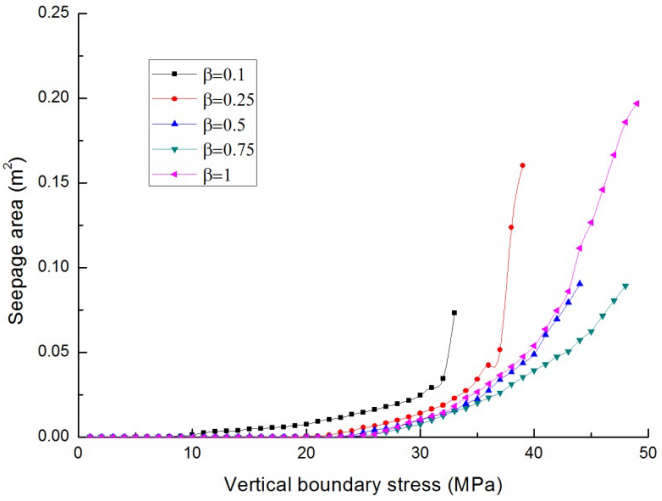

Figure 5: Seepage area under different vertical boundary stress

Fig. 4(c) shows the damage evolution in the drilling area for a tectonic stress coefficient of β=0.5, in which shear damage is first observed at the left and right side of the hole (at Step 28). As the boundary stress increases, the shear fractures propagate, while no tensile fractures can be observed. The damage evolution of the drilling area at β=0.75 is the same (no tensile fractures), and the seepage areas are similar according to Fig. 5. Finally, Fig. 4(e) shows the evolution of the damaged (fractured) area at β=1.0. Here the horizontal boundary stress is equal to the vertical boundary stress. At Step 31, shear damage emerges around the borehole, after which several shear fractures are formed near the borehole (at Step 49). Some tensile damage occurs without forming primary fractures, whilst the area of the seepage area is the largest, reaching to 0.197 m^2.

The length of the longest tensile crack in Fig. 4(a) is 0.176 m, while the longest one in Fig. 4(b) is 0.095 m and no primary tensile cracks are formed in the other three conditions. The increase in the tectonic stress coefficient leads to the decreasing

occurrence of tensile fractures, most likely because the maximum tensile stress above and below the borehole is reduced by the increase of horizontal stress. The V-shaped cracks are caused by shear damage, leading to a complex network of cracks in the rock.

4.2 Damage evolution under varied injecting gas pressure

The damage evolution of the drilling area under different gas injection pressures is considered, as shown in Fig. 6, two specific cases are discussed here: Case A: σ_x=1 MPa, σ_y=10 MPa, and Case B: σ_x=10 MPa, σ_y=10 MPa. The boundary stress is constant during the entire simulation. For both cases, the gas is injected through the borehole; the increment of gas pressure is Δp=0.2 MPa at the inner boundary during the computation; the initial pore pressure is 0 MPa (p_0=0 MPa), and the outer boundary is a non-flowing boundary. The temperature is constant throughout the simulation (T=350 K) and typical for a deep tight sandstone gas reservoir.

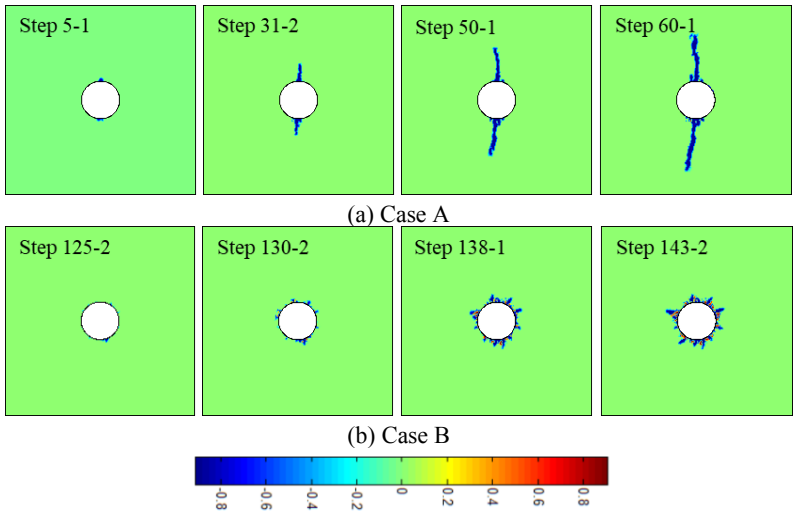

Figure 6: Damage evolution of drilling area under varied injecting gas pressure (positive value denotes shear damage, negative value denotes tensile damage)

Fig. 6(a) shows the evolution of the damage area in Case A. It is seen that tensile damage is first observed above and below the borehole (at Step 5), at which the gas injection pressure was 1 MPa. With the increasing gas injection pressure, the tensile damage propagates toward the top and bottom of the specimen. Finally, two main fractures are formed (at Step 60). Due to the gas pressure at the inner boundary, the tensile stress at both the upper and lower side of the borehole increases, and the shear stress at the left and right sides of the borehole decreases, compared with those in Fig. 4(a). Therefore, tensile fractures propagate deeper into surrounding rocks, shear fractures do not occur.

Fig. 6(b) shows the damage evolution of the drilling area in Case B. A significant tensile damage occurs around the hole (at Step 130) when the injection pressure at the inner boundary reaches 26 MPa. The tensile fractures propagate slowly with the further

increase of gas injection pressure; whilst some shear damage appears around the borehole. Compared with Fig. 4(e), the principle fractures are caused by tensile damage, but the fractures do not propagate deeper into the rock (compared to Fig. 4(e)). This is probably caused by the restrained propagation of tensile damage.

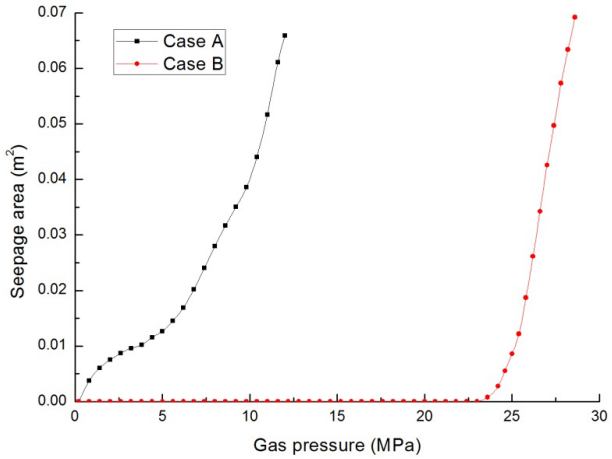

Figure 7: Seepage area development under gas pressure

According to Fig. 7, the seepage area in Case A is similar to that in Case B, which indicates that a smaller tectonic stress coefficient (σ_x/σ_y) has higher efficiency for fracture propagation due to smaller requirement for gas pressure. However, their damage patterns in Cases A and B are different. The deeper and narrower fracture propagation is obtained in Case A, while shorter and wider fracture propagation in Case B.

4.3 Damage evolution under varied gas temperature

Damage evolution under different gas injection temperatures is studied, as shown in Fig. 8, two cases are discussed here: Case A, σ_x=1 MPa, σ_y=10 MPa, and Case B: σ_x=10 MPa, σ_y=10 MPa. For both two cases, the increment of gas temperature is ΔT =1 K at the inner boundary gradually during the simulation. The initial temperature is 350 K (i.e., T_0=350 K), and the outer boundary is thermally insulated. The pore pressure remains constant during all processes (p=20 MPa).

Fig. 8(a) shows the evolution of the damaged area in Case A. The tensile damage spreads to the upper and lower boundaries to form primary fractures, whilst shear damage does not occur. The damage pattern is similar to that in Fig. 6(a) (caused by elevated injection pressure). The thermal stress induced by the increasing gas temperature appears to exacerbate tensile damage.

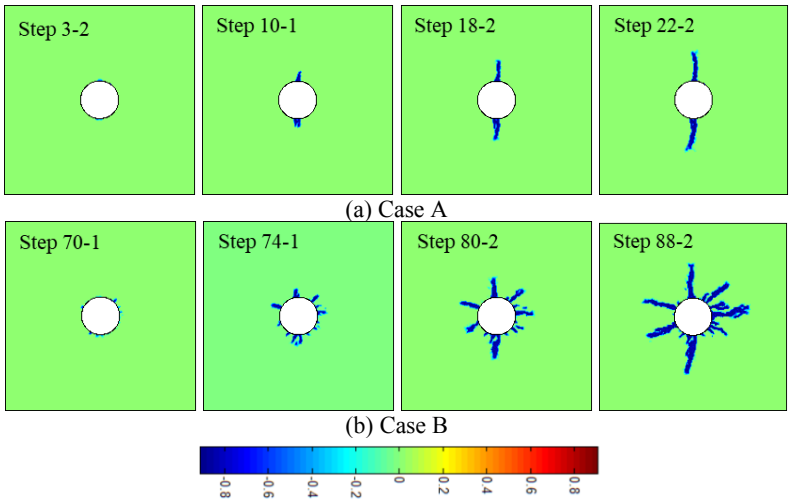

Figure 8: Damage evolution of drilling area under varied gas temperature (positive value denotes shear damage, negative value denotes tensile damage)

As shown in Fig. 9, the seepage area in case A is 0.042 m^2, while the value in Case B is 0.199 m^2, indicating that a larger tectonic stress coefficient (σ_x / σ_y) results in more fractures. However, the damage is more difficult to be observed in Case B than in Case A.

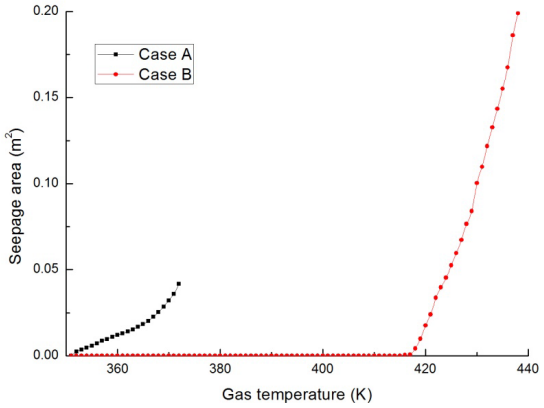

Figure 9: Seepage area evolution under gas temperature

4.4 Damage evolution under coupled TFM conditions

In this part, the effect of simulated gas fracturing on the drilling area is considered through the fully coupled gas-temperature-mechanical boundaries. As shown in Fig. 10, two cases are discussed here: Case A: σ_x=1 MPa, σ_y=10 MPa, and Case B: σ_x=10 MPa, σ_y=10 MPa. For each case and each time step, the increment of gas pressure and gas temperature are Δp=0.2 MPa and ΔT=1 K at the inner boundaries of the model. The

initial gas pressure and gas temperature are p_0=0 MPa, and T_0=350 K. The flow or heat transfer is not permitted in outer boundaries.

In Case A (see Fig. 10(a)), the damage pattern is similar to that of Fig. 6(a) and Fig. 8(a), but its fracture propagation is less restricted, e.g., when the failure occurs in specimens, the coupled boundaries are T=368 K and p=3.6 MPa, whilst the gas pressure in Fig. 6(a) is 12 MPa, the gas temperature in Fig. 8(a) is 372 K. Furthermore, with the same seepage area 0.04 m^2, the coupled boundaries are T= 364 K and p=3.6 MPa (in Fig. 11), while the gas pressure in Fig. 7 is 10 MPa, the gas temperature in Fig. 9 is 372 K.

In Case B (see Fig. 10(b)), the fractures propagate deeper into the surrounding rock compared to that in Fig. 6(b) and Fig. 8(b). The damage occurs at the boundaries when T=405 K and p=11 MPa (see Fig. 10(b)). With the same seepage area 0.07 m^2, the coupled boundaries are T= 401 K and p=10.2 MPa (see Fig. 11), while the gas pressure in Fig. 7 is 28.6 MPa, the gas temperature in Fig. 9 is 427 K.

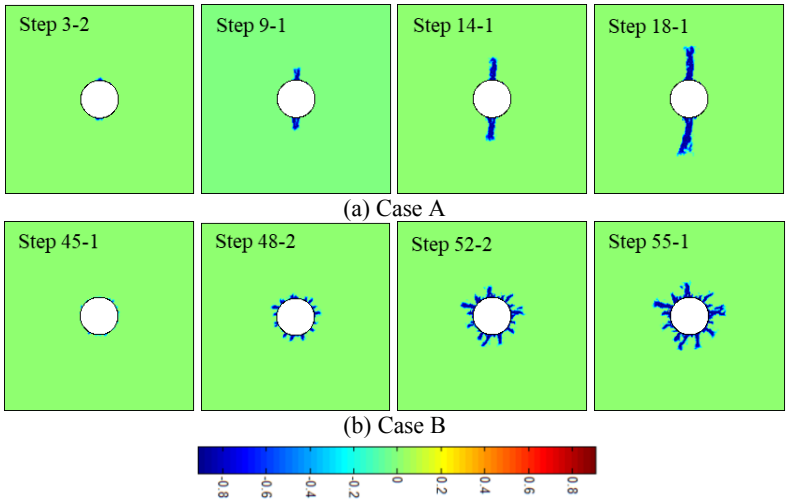

Figure 10: Damage evolution of drilling area under coupled gas-temperature-mechanical boundaries (positive value denotes shear damage, negative value denotes tensile damage)

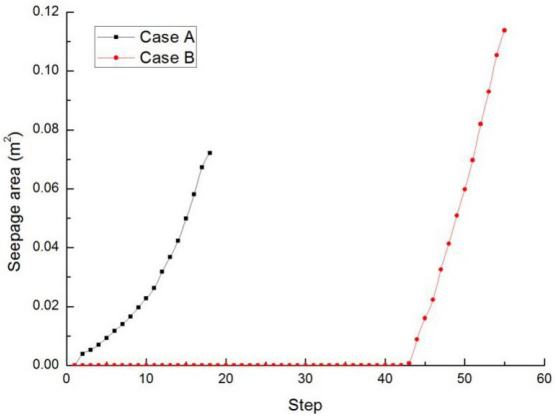

Figure 11: Seepage area evolution under different steps for each step: Δp=0.2 MPa, and ΔT =1 K

It is suggested that the damage can occur in a fully coupled simulation state at lower temperatures and stress rather than in isolated conditions. According to Fig. 11, due to the increase of the horizontal boundary stress, the damage is more difficult to be observed in Case B than in Case A. However, the seepage area at the end of Case B is 0.114 m^2, which is significantly larger than that of Case A (0.072 m^2).

5 Conclusions

The principle of gas fracturing is highly importation for its wide application in tight sandstone gas exploitation. In this paper, a fully coupled TFM model is established. Besides, a damage criterion is introduced to characterize the rock damage, and the damage evolution of borehole under several conditions is discussed. The conclusions can be obtained as follows:

(1) With the increase of the tectonic stress coefficient (β), the maximum tensile crack decreases from 0.176 m (β =0.1) to 0.095 m (β =0.25), and no primary tensile cracks are observed in the last three conditions (β =0.5, 0.75 and 1). This is because maximum tensile stress at the above and below of the borehole is decreased, and tensile fractures are hardly formed. Generally, with the increase of β , the seepage area increases, resulting in an increased volume in shear fractures and the formation of a crushed region. The effect of β on fracture propagation is obtained: with the decrease of β , the relative depth of fractures increases, while the width decreases.

(2) A greater fracture propagation can be caused by a lower β value under the same gas pressure. Similar damage patterns can be obtained under varied gas pressure and gas temperature. The pore pressure and thermal stress have a similar effect on damage evolution, which promotes the propagation of tensile fractures but restrains the propagation of shear fractures.

(3) The fractures zone propagates quickly under the effect of the TFM coupling fields. Therefore, failure and the same seepage area can be obtained easily under TFM coupled conditions.

Funding Statement: This work was supported by the National Natural Science Foundation of China (41977238 and 51804339), the Young Elite Scientists Sponsorship by CAST, the Special Fund for the Construction of Innovative Provinces in Hunan (2019RS2007), the China Postdoctoral Science Foundation (2019T120715 and 2018M640760), the Open Project Fund for State Key Laboratory of Mining Disaster Prevention and Control (MDPC201901) and the Fundamental Research Fund for the Central Universities of CSU (2019zzts675).

Conflicts of Interest: The authors declare that they have no conflicts of interest to report regarding the present study.

References

Cao, Z. Z.; Zhou, Y. J.; Zhang, Q.; Wang, E. Q. (2015): Mechanical analysis of the coupled gas-solid-thermal model during rock damage. *Computers Materials & Continua*, vol. 47, no. 3, pp. 167-179.

Davis, K. M.; Nguyen, M. N.; McClung, M. R.; Moran, M. D. (2018): A comparison of the impacts of wind energy and unconventional gas development on land-use and ecosystem services: an example from the Anadarko Basin of Oklahoma, USA. *Environmental Management*, vol. 61, no. 5, pp. 796-804.

Gu, H. L.; Tao, M.; Li, X. B.; Cao, W. Z.; Li, Q. Y. (2020): Dynamic tests and mechanical model for water-saturated soft coal with various particle gradations. *International Journal of Rock Mechanics & Mining Sciences*, vol. 132, pp. 104386.

Guo, T. K.; Qu, Z. Q.; Gong, D. G.; Lei, X.; Liu, M. (2016): Numerical simulation of directional propagation of hydraulic fracture guided by vertical multi-radial boreholes. *Journal of Natural Gas Science & Engineering*, vol. 35, pp. 175-188.

Hubbert, M.; Willis, D. (1957): Mechanics of hydraulic fracturing. *Transactions of Society of Petroleum Engineers of AIME*, vol. 210, pp. 153-168.

Jia, Y. Z.; Lu, Y. Y.; Elsworth, D.; Fang, Y.; Tang, J. (2018): Surface characteristics and permeability enhancement of shale fractures due to water and supercritical carbon dioxide fracturing. *Journal of Petroleum Science and Engineering*, vol. 165, pp. 284-297.

Li, J.; Li, X. F.; Wang, X. Z.; Li, Y. Y.; Wu, K. L. et al. (2016): Water distribution characteristic and effect on methane adsorption capacity in shale clay. *International Journal of Coal Geology*, vol. 159, pp. 135-154.

Lisjak, A.; Kaifosh, P.; He, L.; Tatone, B. S. A.; Mahabadi, O. K. et al. (2017): A 2D, fully-coupled, hydro-mechanical, FDEM formulation for modelling fracturing processes in discontinuous, porous rock masses. *Computers & Geotechnics*, vol. 81, pp. 1-18.

Liu, J.; Xie, L. Z.; Yao, Y. B.; Gan, Q.; Zhao, P. et al. (2019): Preliminary study of influence factors and estimation model of the enhanced gas recovery stimulated by

carbon dioxide utilization in shale. *ACS Sustainable Chemistry & Engineering*, vol. 7, no. 24, pp. 20114-20125.

Lu, J. L.; Zhao, S. P. (2015): China's natural gas exploration and development strategies under the new normal. *Natural Gas Industry B*, vol. 2, no. 6, pp. 473-480.

Lu, Y. L.; He, M. Q.; Wu, B. Z.; Meng, X. Y. (2020): Experimental and theoretical analysis of hydraulic fracturing and gas fracturing of rock under true triaxial compressions. *Engineering Fracture Mechanics*, vol. 234, 107100.

Ma, D.; Duan, H. Y.; Li, X. B.; Li, Z. H.; Zhou, Z. L. (2019): Effects of seepage-induced erosion on nonlinear hydraulic properties of broken red sandstones. *Tunnelling and Underground Space Technology*, vol. 91, pp. 102993.

Ma, D.; Duan, H. Y.; Liu, W. T.; Ma, X. T.; Tao, M. (2020): Water-sediment two-phase flow inrush hazard in rock fractures of overburden strata during coal mining. *Mine Water and the Environment*, vol. 39, no. 2, pp. 308-319.

Ma, D.; Wang, J. J.; Cai, X.; Ma, X. T.; Zhang, J. X. et al. (2019): Effects of height/diameter ratio on failure and damage properties of granite under coupled bending and splitting deformation. *Engineering Fracture Mechanics*, vol. 220, 106640.

Ma, D.; Wang, J. J.; Li, Z. H. (2019): Effect of particle erosion on mining-induced water inrush hazard of karst collapse pillar. *Environmental Science and Pollution Research*, vol. 26, no. 19, pp. 19719-19728.

Nikolskiy, D. V.; Zammarchi, M.; Mogilevskaya, S. G.; Salvadori, A. (2016): Three-dimensional BEM analysis of stress state near a crack-borehole system. *Engineering Analysis with Boundary Elements*, vol. 73, pp. 133-143.

Osborn, S. G.; Vengosh, A.; Warner, N. R.; Jackson, R. B. (2011): Methane contamination of drinking water accompanying gas-well drilling and hydraulic fracturing. *Proceedings of the National Academy of Sciences*, vol. 108, no. 20, pp. 8172-8176.

Pan, Z. J.; Connell, L. D. (2012): Modelling permeability for coal reservoirs: a review of analytical models and testing data. *International Journal of Coal Geology*, vol. 92, pp. 1-44.

Rabczuk, T.; Belytschko, T. (2004): Cracking particles: a simplified meshfree method for arbitrary evolving cracks. *International Journal for Numerical Methods in Engineering*, vol. 61, no. 13, pp. 2316-2343.

Rabczuk, T.; Gracie, R.; Song, J. H.; Belytschko, T. (2010): Immersed particle method for fluid–structure interaction. *International Journal for Numerical Methods in Engineering*, vol. 81, no. 1, pp. 48-71.

Shen, B. T.; Shi, J. Y. (2016): Fracturing-hydraulic coupling in transversely isotropic rocks and a case study on CO_2 sequestration. *International Journal of Rock Mechanics & Mining Sciences*, vol. 88, pp. 206-220.

Sokolnikoff, I. S.; Specht, R. D. (1956): *Mathematical Theory of Elasticity*. McGraw-Hill, New York.

Wang, T.; Hu, W. R.; Elsworth, D.; Zhou, W.; Zhou, W. B. et al. (2017): The effect of natural fractures on hydraulic fracturing propagation in coal seams. *Journal of Petroleum Science & Engineering*, vol. 150, pp. 180-190.

Wang, X. L.; Shi, F.; Liu, H.; Wu, H. A. (2016): Numerical simulation of hydraulic fracturing in orthotropic formation based on the extended finite element method. *Journal of Natural Gas Science & Engineering*, vol. 33, pp. 56-69.

Wei, C. H.; Zhu, W. C.; Yu, Q. L.; Xu, T.; Jeon, S. (2015): Numerical simulation of excavation damaged zone under coupled thermal-mechanical conditions with varying mechanical parameters. *International Journal of Rock Mechanics & Mining Sciences*, vol. 75, pp. 169-181.

Xia, T. Q.; Zhou, F. B.; Liu, J. S.; Kang, J. H.; Gao, F. (2014): A fully coupled hydro-thermo-mechanical model for the spontaneous combustion of underground coal seams. *Fuel*, vol. 125, pp. 106-115.

Zhang, H. B.; Liu, J. S.; Elsworth, D. (2008): How sorption-induced matrix deformation affects gas flow in coal seams: a new FE model. *International Journal of Rock Mechanics & Mining Sciences*, vol. 45, no. 8, pp. 1226-1236.

Zhang, Q.; Ma, D.; Liu, J. F.; Wang, J. H.; Li, X. B. et al. (2019): Numerical simulations of fracture propagation in jointed shale reservoirs under CO_2 fracturing. *Geofluids*, 2624716.

Zhou, S. W.; Zhuang, X. Y.; Rabczuk, T. (2019): Phase-field modeling of fluid-driven dynamic cracking in porous media. *Computer Methods in Applied Mechanics and Engineering*, vol. 350, pp. 169-198.